Frontiers in Heat and Mass Transfer

Tech Science Press

https://doi.org/10.32604/fhmt.2026.081961

ARTICLE

Heat Transfer Modeling and Failure Analysis of Dry Cooling Systems

Jiaxi Shen and Zhiyun Wang*

School of Energy and Power Engineering, University of Shanghai for Science and Technology, Shanghai, China

*Corresponding Author: Zhiyun Wang. Email: wangzhiyun@usst.edu.cn

Received: 11 March 2026; Accepted: 28 April 2026; Published: 31 August 2026

ABSTRACT: This study focuses on the modeling and performance prediction of the condensation heat transfer process within an ACC system of a 100 MW unit. A one-dimensional physical model was established, and solutions were obtained using an iterative numerical method based on the first law of thermodynamics. The core of this work involves precise modifications to the heat transfer coefficient. Firstly, the Shah correlation for horizontal tube condensation was improved by incorporating the air mass fraction and the Jakob number to quantify the impact of non-condensable gases. Secondly, to assess the influence of the pipe installation angle, an inclination factor (I), which integrates the Eötvös number, Lockhart-Martinelli parameter, and a modified Froude number, was introduced to correct the heat transfer coefficient for inclined tubes. Furthermore, the relationship between the void fraction and steam dryness was investigated. The research provides a theoretical model and analytical tools for diagnosing typical operational issues in ACCs, such as backpressure optimization and environmental adaptability. It offers valuable guidance for enhancing the operational efficiency and reliability of air-cooled islands under varying conditions.

KEYWORDS: ACC; heat transfer model; performance prediction; heat transfer coefficient modification; inclination factor

1 Introduction

Energy is fundamental to human survival and development. The progress of human society is inextricably linked to the emergence of high-dryness fraction energy sources and the development of advanced energy technologies. With the rapid economic development, traditional energy sources such as coal, petroleum, and natural gas are increasingly failing to meet contemporary societal demands due to depleting reserves, increasing extraction challenges, and exacerbated environmental pollution. Finding clean energy sources with high energy density to replace traditional fossil fuels is a crucial agenda in the energy sector development of various countries.

Amid growing global energy demand and the pursuit of "dual carbon" goals, the issues of energy conservation, consumption reduction, and sustainable water resource utilization in thermal power plants, as primary energy suppliers, have become increasingly prominent. Traditional wet cooling units rely heavily on circulating water for condenser cooling, facing severe water resource constraints in coal-rich but water-scarce regions (e.g., northwestern China). Air-Cooled Condenser (ACC) technology, which directly or indirectly uses air to cool turbine exhaust steam, can reduce plant water consumption by over 80%, making it the preferred solution for thermal power construction in arid areas.

However, ACC systems have significant drawbacks: increased backpressure leads to lower heat transfer efficiency, limiting unit output by 15%–20% during high summer temperatures; they are highly sensitive to

Copyright © 2026 The Authors. Published by Tech Science Press. This work is licensed under a Creative Commons Attribution 4.0 International License, which permits unrestricted use, distribution, and reproduction in any medium, provided the original work is properly cited.

ambient wind speed and temperature fluctuations, resulting in insufficient operational stability. Particularly under high ambient temperatures, the reduced temperature difference between air and steam for heat transfer causes a sharp decline in condensation efficiency, severely impacting plant economy and power supply reliability. Therefore, research on enhancing the condensation process in ACCs holds significant engineering value for improving system energy efficiency and ensuring grid stability.

In industrial contexts, the condensation heat transfer process involving a working fluid completely free of non-condensable components is termed pure working fluid condensation. As a benchmark for studying condensation heat transfer characteristics in the presence of non-condensable gases, the analysis of pure working fluid condensation characteristics inside horizontal tubes has long attracted significant attention from researchers worldwide.

In the early 20th century, the German scientist Ernst Nusselt conducted pioneering theoretical analysis in 1916 on laminar film condensation of pure steam on vertical walls and outside horizontal tubes. The Nusselt theory assumed laminar flow in the liquid film and neglected the effects of vapor velocity and inertial forces. His theoretical solution provided the fundamental physical framework for understanding condensation heat transfer and remains the theoretical starting point for condenser design [1]. In 1979, Shah integrated extensive experimental data to propose a general semi-empirical correlation applicable to various working fluids over a wide parameter range, which is widely used in engineering design [2]. In 2015, Ren Bin and others from East China University of Science and Technology used direct temperature measurement methods to experimentally propose flow pattern transition criteria and heat transfer correlations for steam condensation containing non-condensable gases inside horizontal tubes. They indicated that under high Reynolds number conditions, stronger gas-liquid interfacial shear can partially mitigate the negative impact of non-condensable gases on condensation heat transfer [3]. In 2025, a team from Shanghai Jiao Tong University conducted detailed simulations of the methanol condensation process in the carbon dioxide hydrogenation to methanol process using the VOF model and Lee phase change model. They found that the heat transfer coefficient peaked at a methanol vapor dryness fraction between 0.87 and 0.95, and that increasing the mass flux shifted the peak to the right and improved the liquid film distribution uniformity [4]. To date, numerous research findings on gas-liquid two-phase flow patterns and condensation heat transfer characteristics inside horizontal tubes have been published.

In the study of gas-liquid two-phase flow in pipes, accurately predicting pressure drop is a core issue in system design and optimization. Since Lockhart and Martinelli proposed their semi-empirical correlation in 1949, the Lockhart-Martinelli method has become one of the foundational models for analyzing and predicting frictional pressure drop in two-phase flows [5]. This method correlates the frictional pressure drop gradients of two-phase flows by introducing the Martinelli parameter (Xtt) and categorizes the flow into four typical regimes based on the flow patterns (laminar or turbulent) of the gas and liquid phases flowing alone in the pipe. This provides a systematic framework for pressure drop calculation under various flow conditions. The model is valued for its simple form, clear physical significance, and is particularly suitable for rapid engineering estimation of two-phase flow systems where detailed flow pattern information is lacking.

However, the classical Lockhart-Martinelli method often exhibits significant prediction inaccuracies when applied to complex conditions such as high pressure, microchannels, or scenarios with rapidly changing flow regimes. To address this limitation, Chisholm built upon the Lockhart-Martinelli framework by introducing a C coefficient that accounts for the interfacial interaction between the two phases, proposing the famous Chisholm correlation. This significantly improved the prediction accuracy for specific flow regimes (such as annular and stratified flows) [6]. Subsequently, numerous researchers have focused on empirically modifying and adapting the C coefficient for different media, pipe geometries, and inclination angles.

Although the development of computational fluid dynamics (CFD) has laid a solid foundation for accurately simulating the internal working conditions and external airflow and heat transfer in air-cooled islands, existing research has largely overlooked the quantitative impact of non-condensable gases (such as air) within condenser tubes and their dynamic distribution on heat transfer performance. To address this critical gap, this study aims to establish a coupled numerical model that accounts for the flow and heat transfer of steam-gas mixtures inside the tubes, systematically analyzing how different air mass fractions and distribution non-uniformity weaken the overall heat transfer coefficient and vacuum level. We will focus on investigating how inlet steam dryness fraction and fan operation strategies influence the accumulation patterns of non-condensable gases. By revealing the evolution of thermal performance in air-cooled islands under gas-containing conditions, this work aims to provide a new theoretical basis for enhancing operational energy efficiency and developing effective air extraction strategies.

2 Governing Equations and Numerical Methods

2.1 Governing Equations

Fig. 1 shows a one-dimensional schematic of the steam condensation process in a single condenser tube bundle. To describe the coupled variations of condensation, non-condensable gas accumulation, and pressure drop, a one-dimensional steady-state model is established along the tube axial direction z. For a differential control volume, the mass conservation equations are written as [7]:

$$\frac{dm_w}{dz} = 0 \tag{1}$$

$$\frac{dm_a}{dz} = S_a \tag{2}$$

where m_w is the mass flow rate of water, m_a is the mass flow rate of air and S_a is the source term of non-condensable gas. Under normal operating conditions, $S_a = 0$; under leakage conditions, $S_a \neq 0$.

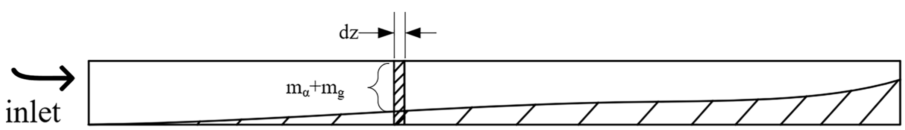

Figure 1: One-dimensional schematic diagram of the steam condensation process of a single tube bundle.

The total mass flow rate is expressed as: $m = m_w + m_a$. The local dryness fraction is defined as: $x = \frac{m_g}{m_w}$, where m_g is the mass flow rate of steam and the air mass fraction is defined as: $\omega_a = \frac{m_a}{m}$.

The heat released by steam condensation is transferred through the tube wall to the external cooling air. Neglecting axial heat conduction in both the wall and the fluids, the one-dimensional energy balance for each control volume is written as [8]:

$$\frac{d}{dz}\left(m_g h_g + m_l h_l + m_a h_a\right) = -q' \tag{3}$$

where h_g, h_l and h_a are the specific enthalpies of steam, condensate, and air, respectively, and q' is the heat transfer rate per unit tube length. The values of h_g and h_l are the specific enthalpy of saturated steam at the corresponding pressure. h_a is obtained by multiplying the specific heat capacity by the temperature. The same heat transfer rate can also be evaluated using the overall heat transfer relation [9]:

$$q' = KP(T_s - T_a) \tag{4}$$

where K is the overall heat transfer coefficient, P is the equivalent heat transfer perimeter, T_s is the local steam saturation temperature corresponding to the local pressure, and T_a is the air temperature outside the tube segment. The calculation of K is expressed by the following formula [10]:

$$\frac{1}{K} = \frac{n_f A_f + A_b}{h_i A_i} + \frac{d_o}{2\lambda} \ln \frac{d_o}{d_i} + \frac{1}{h_o} \tag{5}$$

where λ represents the thermal conductivity of the pipe wall, n_f denotes the efficiency of the fins, A_f is the total area of the fins, A_b is the exposed area of the base pipe, A_i is the heat exchange area within the pipe, h_i and h_o are the convective heat transfer coefficients inside and outside the pipe, respectively, d_i and d_o are the diameters inside and outside the pipe, respectively.

To couple the condensation process with the hydraulic behavior, the axial pressure variation in the condenser tube is described by [11]:

$$\frac{dp}{dz} = \left(\frac{dp}{dz}\right)_f + \left(\frac{dp}{dz}\right)_a + \left(\frac{dp}{dz}\right)_g + p_{local} \tag{6}$$

where the terms on the right-hand side represent the frictional, accelerational, gravitational, and local pressure drop components, respectively.

The frictional pressure drop of the two-phase flow is calculated using the Chisholm-modified Lockhart-Martinelli method [12]:

$$\left(\frac{dp}{dz}\right)_f = \varnothing_l^2 \cdot \frac{f_l}{D} \cdot \frac{1}{2}\rho_l v_l^2 \tag{7}$$

or equivalently,

$$\left(\frac{dp}{dz}\right)_f = \varnothing_g^2 \cdot \frac{f_g}{D} \cdot \frac{1}{2}\rho_g v_g^2 \tag{8}$$

where ϕ_l^2 and ϕ_g^2 represent the liquid-phase multiplier and the gas-phase multiplier, respectively, which can be calculated using the Lockhart-Martinelli parameters. The Lockhart-Martinelli parameter is defined as [13]:

$$X_{tt} = \left(\frac{u_l}{u_g}\right)^{0.1} \times \left(\frac{\rho_g}{\rho_l}\right)^{0.5} \times \left(\frac{1}{x} - 1\right)^{0.9} \tag{9}$$

For the calculation of the all-liquid friction factor f_l, appropriate formulas are selected based on the flow regime. Under laminar flow conditions, the Hagen-Poiseuille equation is used [14]:

$$f_l = \frac{64}{Re} \tag{10}$$

Under turbulent flow conditions, the Haaland equation is employed [15]:

$$f_l = \frac{1}{\left(1.8 \times \log_{10}\left(\left(\frac{\varepsilon}{3.7D}\right)^{1.11} \cdot 11 + \frac{6.9}{Re}\right)\right)^2} \tag{11}$$

where ε is the pipe absolute roughness, D is the pipe inner diameter, and Re is the liquid-phase Reynolds number.

The accelerational pressure drop term is written as [16]:

$$\left(\frac{dp}{dz}\right)_a = -\frac{d}{dz}\left[G^2\left(\frac{x^2}{a\rho_g} + \frac{(1-x)^2}{(1-a)\,\rho_l}\right)\right] \tag{12}$$

where G is the mass flux, x represents the dryness of steam, a represents the void ratio, and ρ_g and ρ_l, respectively denote the densities of the gas phase and the liquid phase.

The gravitational pressure drop term is written as [17]:

$$\left(\frac{dp}{dz}\right)_g = \left[a\rho_g + (1-a)\,\rho_l\right] gsin\theta \tag{13}$$

where θ is the tube inclination angle.

The local resistance pressure drop refers to the energy loss caused by collisions or vortex formation of fluid particles due to changes in flow cross-section or flow direction. In this model, the primary location generating local resistance is the T-junction where the main flow splits into a branch. The local resistance coefficient can be calculated using the following formula [18]:

$$k_b = 1.2 + \left[0.95\left(\frac{M_b}{M_m}\right)^2 - 1.3\frac{M_b}{M_m}\right] \tag{14}$$

Assuming that phase change occurs only within the condenser tube bundles, the local resistance pressure drop at this location can be calculated using the single-phase local resistance pressure drop formula [19]:

$$p_{local} = k_b \cdot \frac{1}{2}\rho_g \cdot \left(\frac{M_b}{\rho_g \cdot A}\right)^2 \tag{15}$$

where M_b is the mass flow rate in the branch; M_m is the mass flow rate in the main pipe; ρ_g is the gas phase density; $A = \frac{\pi d_i^2}{4}$ is the pipe cross-sectional area; d_i is the pipe inner diameter.

Eqs. (1)–(3) and (6) form a closed one-dimensional system of equations. To close the one-dimensional governing equations, the following boundary conditions are imposed:

$$p\,(0) = p_{in}, x\,(0) = x_{in}, \omega_a\,(0) = \omega_{a\,in}, M_b\,(0) = M_{b\,in}, p_1\,(L) = p_2\,(L) = \ldots = p_n\,(L)$$

where p_{in}, x_{in}, $\omega_{a\,in}$, and $M_{b\,in}$ denote the inlet pressure, steam dryness fraction, air mass fraction, and mass flow rate at the branch inside the pipe, respectively. The pressure at the outlets of each branch pipe is equal.

2.2 Numerical Procedure and Convergence Criteria

The governing equations are solved sequentially over the control volumes along the flow direction of the condenser tube bundle. The differential equations are discretized using the trapezoidal method, which provides second-order accuracy. For each branch, an initial inlet mass flow rate is specified first. Based on the inlet boundary conditions, the outlet state parameters of each control volume are calculated successively using the trapezoidal method. Once convergence is achieved for the current control volume, its outlet parameters are taken as the inlet conditions for the next one, and the calculation proceeds along the flow direction until the outlet parameters of the last control volume are obtained. Since all parallel branches share the same outlet boundary, their outlet pressures should be identical. Therefore, the inlet mass flow rates of the branches are corrected according to the deviation between each branch outlet pressure and the average outlet pressure, and the calculation is repeated until the outlet pressures of all branches are equal within a prescribed tolerance.

The numerical procedure is summarized as follows:

(1) a control-volume discretization model is established along the flow direction of the condenser tube bundle, and the governing equations are discretized by integral formulation using the trapezoidal method;
(2) the inlet boundary conditions and an initial guess of the inlet mass flow rate are specified for each branch;
(3) for each individual branch, the governing equations are solved sequentially control volume by control volume, and the outlet parameters of the previous control volume are taken as the inlet conditions for the next one;
(4) after all control volumes have been calculated, the outlet pressure of each branch is obtained;
(5) the outlet pressures of all branches are then compared, and the inlet mass flow rates are corrected according to the deviation between each branch outlet pressure and the average outlet pressure;
(6) the above procedure is repeated until the outlet pressures of all branches satisfy a unified convergence criterion.

The convergence criteria are defined as:

$$\left|\frac{x_i^{(k+1)} - x_i^{(k)}}{x_i^{(k)}}\right| < \varepsilon_x, \left|\frac{p_i^{(k+1)} - p_i^{(k)}}{p_i^{(k)}}\right| < \varepsilon_p, \max_j \left|p_{out,j} - \overline{p}_{out}\right| < \varepsilon_f$$

where ε_x, ε_p and ε_f are the prescribed tolerances for dryness fraction, pressure, and flow-distribution iteration, respectively.

2.3 Modification of Steam Condensation Heat Transfer Model with Non-Condensable Gases

2.3.1 Correction of Condensation Heat Transfer Coefficient in Horizontal Tubes

This study employs the Shah condensation correlation as the fundamental model for calculating the in-tube flow condensation heat transfer coefficient. Its basic expression is [20]:

$$h_{Shah} = h_l \cdot \left(1 + \frac{3.8}{Z^{0.95}}\right) \tag{16}$$

where h_{Shah} represents actual condensation heat transfer coefficient, h_l represents pure liquid phase (no phase change) heat transfer coefficient, calculated by the Dittus-Boelter equation: $h_l = 0.023 \cdot Re_l^{0.8} \cdot Pr_l^{0.4} \cdot \frac{k_l}{D}$, Z represents dimensionless parameter, defined as: $Z = \left(\frac{1}{x} - 1\right)^{0.8} \cdot Pr_l^{0.4}$, where x represents dryness fraction (gas phase mass fraction), Pr_l represents liquid Prandtl number.

To account for the influence of non-condensable gases on the condensation process, this study introduces correction terms for air mass fraction (ω_a) and Jakob number (J_a) based on the Shah correlation [21]:

$$h_i = h_{Shah} \cdot (1 - \omega_a)^{0.9} \cdot exp\,(-0.12 \cdot J_a) \tag{17}$$

where the Jakob number is defined as $J_a = \frac{c_p \Delta T}{r}$, used to characterize the competing effect between sensible and latent heat.

2.3.2 Correction of Condensation Heat Transfer Coefficient in Inclined Tubes

For the condensation process inside inclined tubes, the inclination coefficient I proposed by Yang is used to correct the horizontal tube heat transfer coefficient [22]:

$$I = \frac{h}{h_{\theta=0^\circ}} \tag{18}$$

here, I is defined as the ratio of the heat transfer coefficient h at a specific inclination angle to the heat transfer coefficient at the horizontal position ($\theta = 0^\circ$).

In stratified flow patterns, gas-liquid shear force and gravity are the main factors affecting liquid film thickness. Wallis proposed using a modified Froude number to characterize the relative importance of gas-liquid shear force and gravity. This dimensionless number can be used to distinguish between annular flow and stratified flow in inclined tubes:

$$F = \sqrt{\frac{\rho_g}{(\rho_l - \rho_g)}}\frac{J_g}{\sqrt{dgcos\theta}} \tag{19}$$

here, J_g is the superficial gas velocity.

The flow pattern discrimination criteria and the corresponding heat transfer coefficient calculations are as follows:

When $F \geq 1.3$:

$$h_{cal} = h_{Shah,\,\theta=0^\circ} \tag{20}$$

When $F < 1.3$:

$$h_{cal} = I \cdot h_{Shah,\ \theta=0^\circ} \tag{21}$$

The specific expression for the inclination coefficient I is:

$$I = 1 + \frac{0.02 \cdot {E_o}^{0.95}}{{X_{tt}}^{0.136} \cdot F^{1.477}} \sin(2.8\theta) \tag{22}$$

here the Eötvös number (E_o) is defined as:

$$E_o = \frac{(\rho_l - \rho_g)gd^2}{\sigma_l} \tag{23}$$

According to research findings by Ge Jianying (Inner Mongolia University of Science and Technology), the heat transfer coefficient in inclined pipes initially increases and then decreases with increasing inclination angle, reaching a maximum near $\theta = 30^\circ$. Considering the actual installation conditions of the equipment in practical engineering, this model uses an inclination angle of $\theta = 60^\circ$ for calculations.

2.3.3 Void Fraction

Due to the velocity slip between the gas and liquid phases, the void fraction (α) is not equal to the vapor dryness fraction (x). The less dense gas phase typically flows faster than the denser liquid phase. This phenomenon is characterized by the following relationship [23]:

$$\frac{1-\alpha}{\alpha} = 0.28\left(\frac{1-x}{x}\right)^{0.64}\left(\frac{\rho_g}{\rho_l}\right)^{0.36}\left(\frac{\mu_l}{\mu_g}\right)^{0.07} \tag{24}$$

3 Results and Discussion

The local layout of the investigated air-cooled condenser (ACC) system is illustrated in Fig. 2. The distributor pipe of the air-cooled island is divided into a front section and a rear section. The front section has an inner diameter of 2.02 m and a length of 15 m, while the rear section has an inner diameter of 1.62 m and a length of 21 m. Starting from the inlet of the distributor pipe, condenser tube bundles are symmetrically arranged on both sides at intervals of 1 m, excluding the pipe ends, resulting in a total of 70 tube bundles.

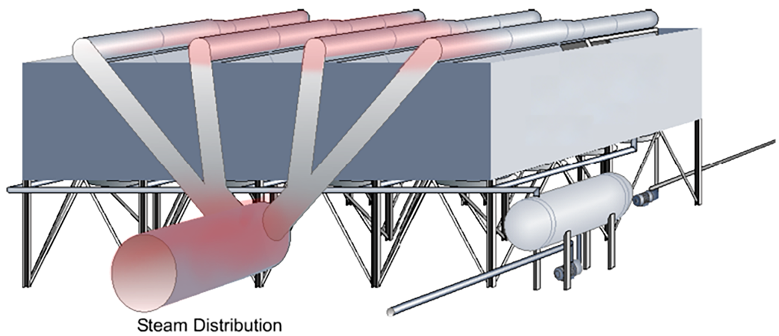

Figure 2: Overall model of the power plant air-cooled island.

As shown in Fig. 3, each condenser tube has an outer diameter of 25 mm and a wall thickness of 1.5 mm. Annular fins are installed on the tube surface, with a fin thickness of 3 mm, fin spacing of 17 mm, and fin radius of 35 mm. After entering the air-cooled island through the main steam duct, the exhaust steam is distributed into four distributor pipes and subsequently flows into the condenser tube bundles, where it condenses and drains into the condensate tank.

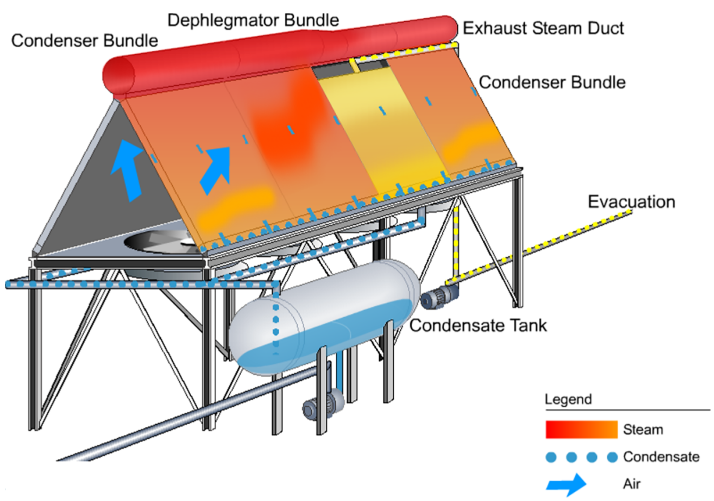

Figure 3: Demonstration of local working fluid operation in the power plant air-cooled island.

In this study, the flow distribution from the main steam duct to the distributor pipes is neglected. Only the steam flow and condensation process within a single distributor pipe and its connected condenser tube bundles are simulated. It is further assumed that no condensation occurs within the distributor pipe itself, and phase change takes place exclusively inside the condenser tubes.

Since the actual air-cooled island structure is symmetrical on both sides, the simulation process adopts the conditions of one side to simplify the simulation. Fig. 4 is a plan view schematic diagram of the steam flow inside the condenser tubes on one side. The steam enters each condenser tube bundle through the distribution pipe and finally the condensate water flows into the condensate tank from below. Each condenser tube bundle is evenly divided into 100 segments, and the center position of each segment is taken, and the average value is used as the recorded result for that segment, as shown in the first condenser tube bundle in the figure. Finally, all the recorded results of the condenser tube bundles are plotted as a cloud chart to verify whether there is a heat transfer failure problem.

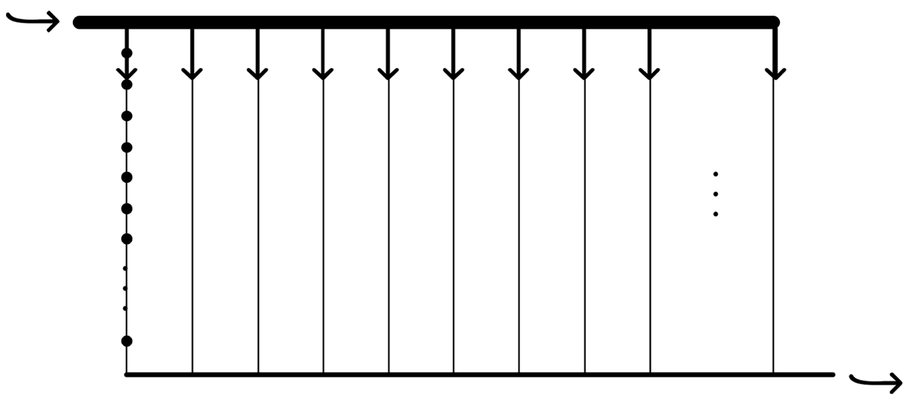

Figure 4: Schematic diagram of steam flow pattern.

As shown in Fig. 5, the simulated values of heat dissipation and condensate flow rate are generally slightly lower than the measured values. The maximum error of heat dissipation occurs under Summer Condition 2, reaching 4.92%, while the minimum error occurs under Summer Condition 1, at 3.61%. For the condensate flow rate, the maximum error also appears under Summer Condition 2, at 3.79%, whereas the minimum error is observed under Rated Condition 1, at 2.49%. The relative errors between simulated and measured values under all conditions are controlled within approximately 5%. Therefore, the proposed model exhibits high predictive accuracy.

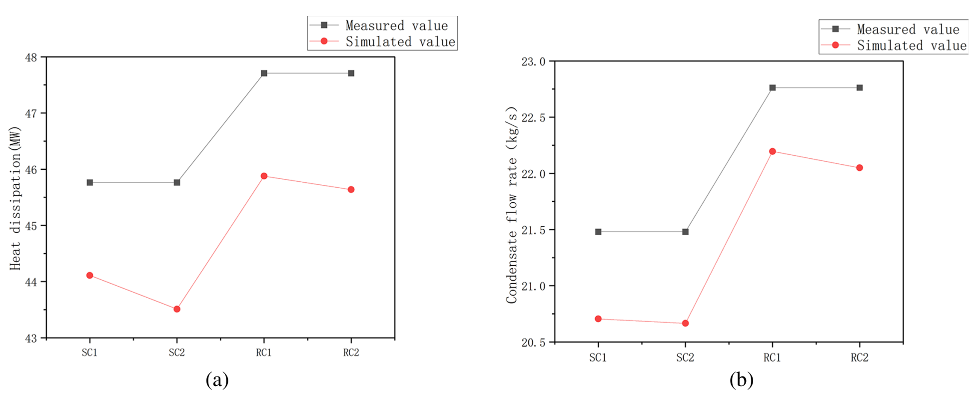

Figure 5: (**a**) Comparison of measured and simulated heat dissipation under different conditions; (**b**) Comparison of measured and simulated condensate flow rate under different conditions.

Furthermore, in terms of consistency and stability, the variation in errors across different operating conditions is relatively small, and no abrupt increase in error is observed under any specific condition. This indicates that the model maintains good stability and applicability under various operating conditions.

To evaluate the applicability of the proposed model under practical operating conditions, numerical simulations were performed by varying the outlet velocity of selected axial flow fans. One or several condenser tube bundles located above a specific fan were chosen, and the corresponding fan outlet velocity was reduced to simulate local operating failures that lead to a degradation in heat transfer performance.

The simulation results obtained under these faulty conditions were compared with those under normal operating conditions. The distributions of vapor dryness fraction, air mass fraction, and pressure drop along the condenser tube bundles were recorded, and contour plots were generated to visualize the variations in thermal–hydraulic performance.

Figs. 6–8 are generated based on the data obtained under the condition that the unit is operating normally, with a steam flow rate of 18 t/h and a fan outlet speed of 10 m/s.

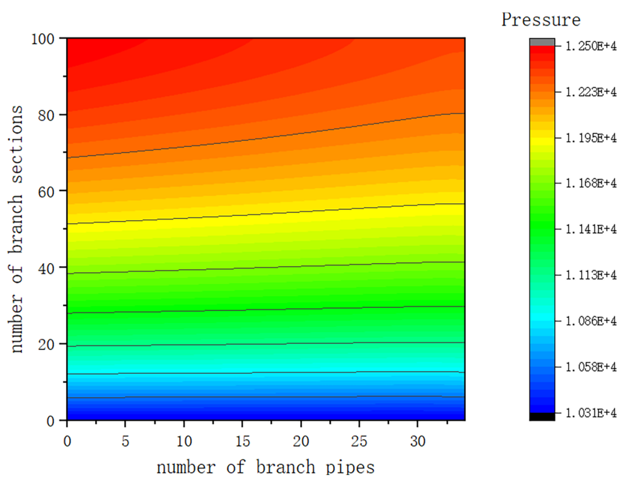

Figure 6: Pressure distribution of the condensing tube bundle.

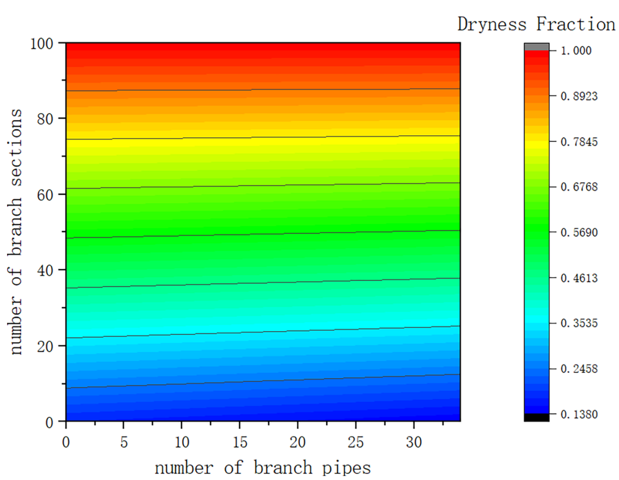

Figure 7: Dryness fraction distribution of the condensing tube bundle.

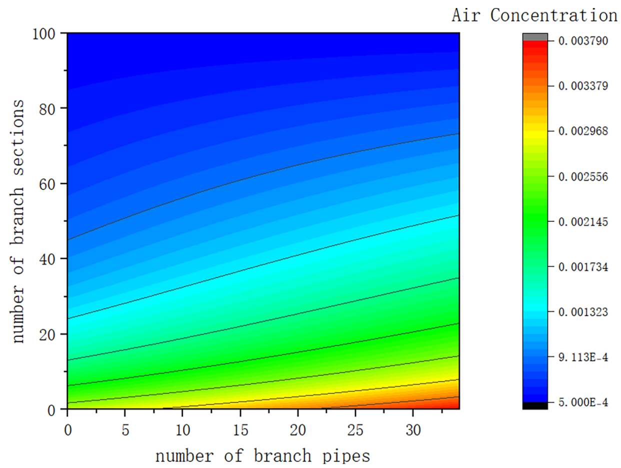

Figure 8: Air concentration distribution of the condensing tube bundle.

After accounting for the pressure drop in the distribution pipe and the local pressure drop at the entrance from the distribution pipe into the condenser tubes, the inlet pressures of the condenser tube bundles are not identical. The first condenser tube bundle has the highest inlet pressure, and the pressure gradually decreases for the subsequent bundles. Since the condensate and uncondensed steam from all condenser tube bundles are ultimately discharged into the same container, the outlet pressure of all condenser tube bundles can be considered the same, which is generally consistent with the results shown in Fig. 6.

Due to the decreasing pressure difference between the tubes of the condenser bundles, the simulated steam flow into each condenser bundle also decreases successively. Therefore, under the same condensation path length, heat transfer conditions, and steam dryness of the inlet, the condensation degree of the steam in the last condenser bundle is the highest. This result is shown in Fig. 7, the lower right area of the figure corresponds to the minimum steam dryness.

The air content of the steam entering each condenser tube bundle is identical. However, in the condenser tube bundles where the condensation degree is higher, the proportion of air in the total gas mixture inside the tube becomes larger, indicating a higher air mass fraction. This phenomenon is consistent with the results shown in Fig. 8.

Increase the steam flow and draw the cloud charts of dryness, pressure and air mass fraction under normal operating conditions, as shown in Figs. 9–11.

Figs. 9–11 are like Figs. 6–8. The increase in steam flow leads to a decrease in the degree of steam condensation within the condenser tube bundle, an increase in the pressure at the tube bundle outlet, and a decrease in the concentration of air within the tube bundle.

During the simulation, the fan's air outlet speed was adjusted multiple times to make the condensation degree corresponding to the steam flow rate approximately consistent with that under the condition of a steam flow rate of 18 t/h and an air outlet speed of 10 m/s. The dryness at the outlet of the condensation tube bundle and the concentration of the outlet air were recorded and a Fig. 12 was drawn.

As shown in the Fig. 12, this model can enhance the heat exchange performance by increasing the outflow speed of the fan, ensuring a consistent condensation effect even when the steam flow increases. This demonstrates that this model has certain repeatability and accuracy in its simulation results.

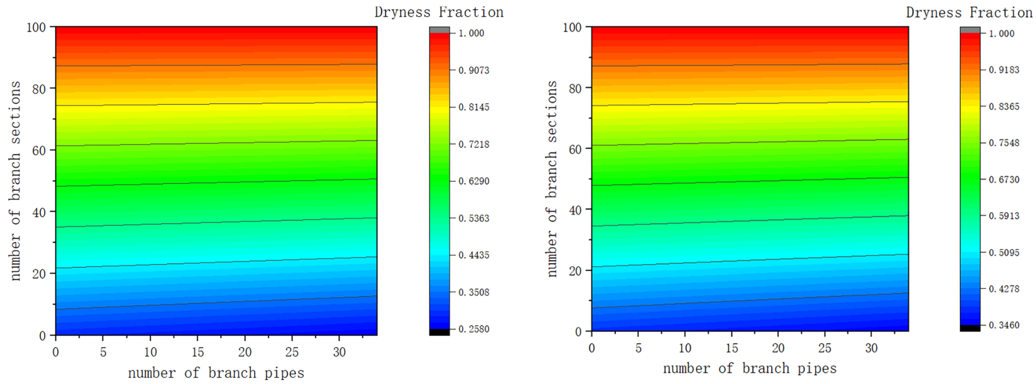

(a) (b)

Figure 9: (**a**) Dryness fraction distribution of the condensing tube bundle at a steam flow rate of 21 t/h under normal operating conditions; (**b**) Dryness fraction distribution of the condensing tube bundle at a steam flow rate of 24 t/h under normal operating conditions.

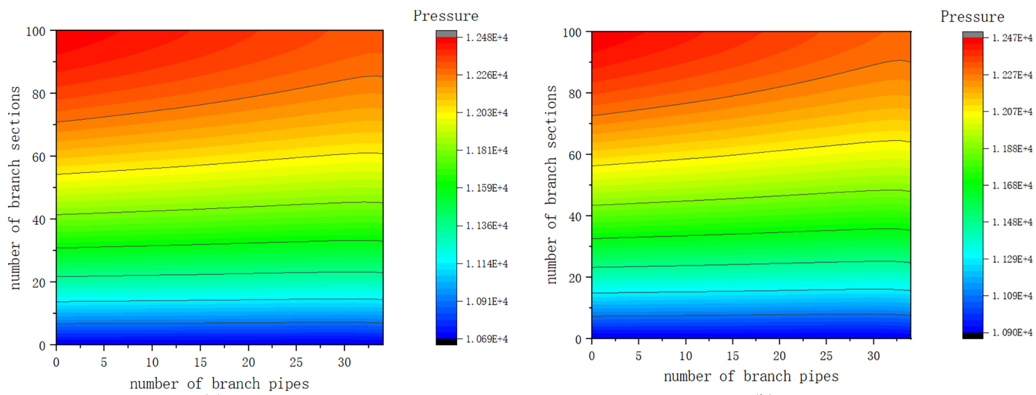

(a) (b)

Figure 10: (**a**) Pressure distribution of the condensing tube bundle at a steam flow rate of 21 t/h under normal operating conditions; (**b**) Pressure distribution of the condensing tube bundle at a steam flow rate of 24 t/h under normal operating conditions.

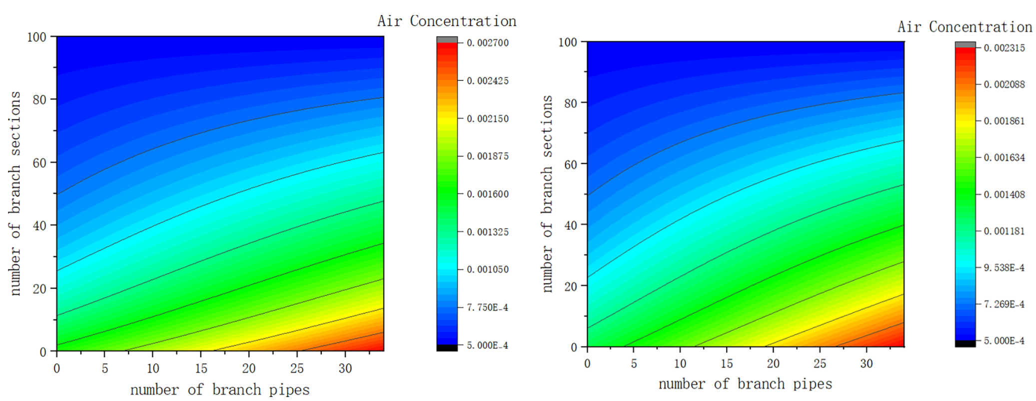

(a) (b)

Figure 11: (**a**) Air concentration distribution of the condensing tube bundle at a steam flow rate of 21 t/h under normal operating conditions; (**b**) Air concentration distribution of the condensing tube bundle at a steam flow rate of 24 t/h under normal operating conditions.

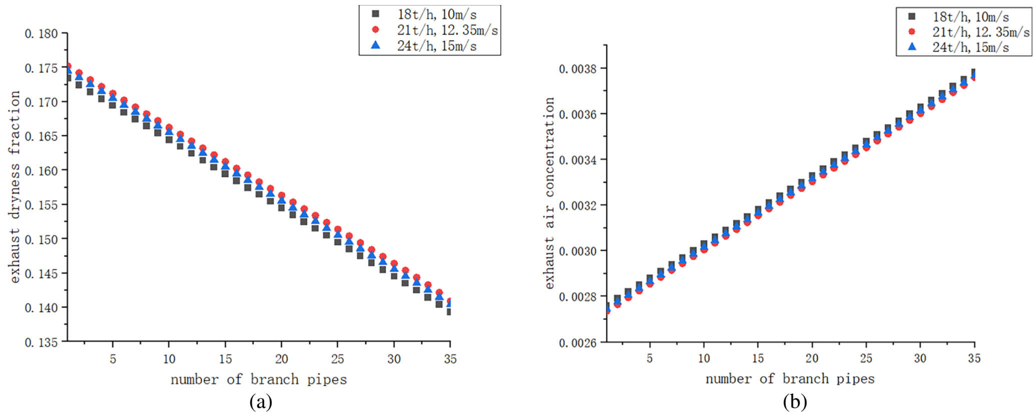

Figure 12: (**a**) The exhaust dryness fraction of the condenser tubes under different conditions; (**b**) The exhaust air mass fraction of the condenser tubes under different conditions.

Under the conditions of a steam flow rate of 18 t/h and a fan outlet velocity of 10 m/s, increase the air mass fraction at the inlet (from 0.5‰ to 1‰) and draw the distribution charts of dryness, pressure and air mass fraction, as shown in Figs. 13–15.

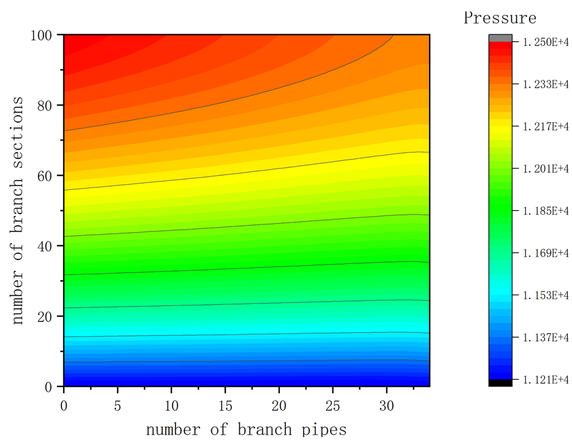

Figure 13: Pressure distribution of the condensing tube bundle.

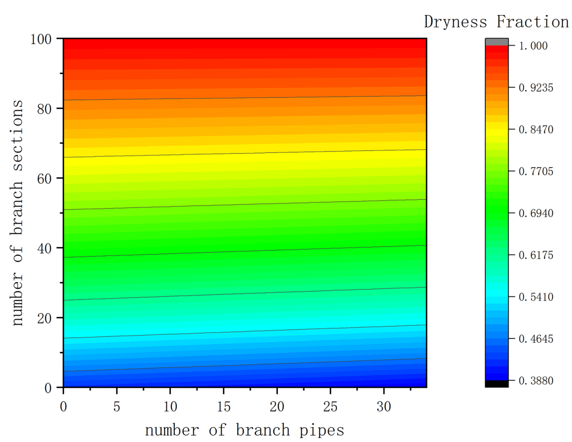

Figure 14: Dryness fraction distribution of the condensing tube bundle.

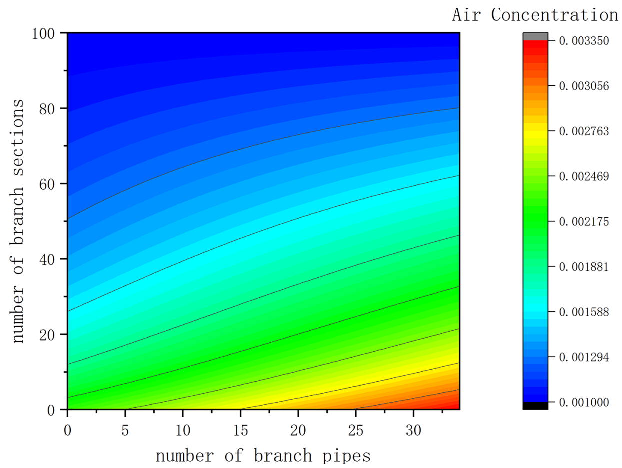

Figure 15: Air concentration distribution of the condensing tube bundle.

When comparing Figs. 6–8 with Figs. 13–15, where the inlet air mass fraction is increased (from 0.5‰ to 1‰), the model shows a systematic shift in the air mass fraction distribution. Specifically, the overall air mass fraction level within the tube bundles increases, and the accumulation effect becomes more pronounced, while the condensation degree (dryness fraction) is correspondingly reduced. This demonstrates that the model can dynamically respond to changes in inlet air mass fraction and accurately reflect the coupling between condensation and gas accumulation.

Regarding sensitivity, the results indicate that the model outputs are moderately sensitive to the assumed inlet air mass fraction. An increase in inlet air mass fraction leads to:

(1) a higher local air mass fraction throughout the tube bundle,
(2) a reduction in condensation efficiency (higher outlet dryness fraction), and
(3) a redistribution of the thermal–hydraulic field.

However, the overall spatial patterns (e.g., downstream accumulation of air and monotonic condensation behavior) remain consistent, indicating that the model maintains robust structural behavior while still capturing quantitative variations due to different air mass fraction levels.

Therefore, the model is not only capable of representing the spatial distribution of non-condensable gases, but also sufficiently sensitive to variations in air mass fraction, allowing it to simulate realistic operating scenarios and assess the impact of air ingress on system performance.

When a leakage occurs at the 80th section of the 20th tube bundle, with a leakage rate of 0.0005 kg/s, the air mass fraction distribution diagram as shown in Fig. 16 can be obtained.

As can be seen from Fig. 16, significant air accumulation occurred in the latter half of the second ten condenser tubes. The air quality fraction at the outlet increased from 0.5‰ at the inlet to 3.68%.

Figs. 17–19 are generated based on the data collected when abnormal operating conditions occurred in the 13th and 14th condenser bundles of the unit, with a steam flow rate of 18 t/h and a fan outlet speed of 10 m/s.

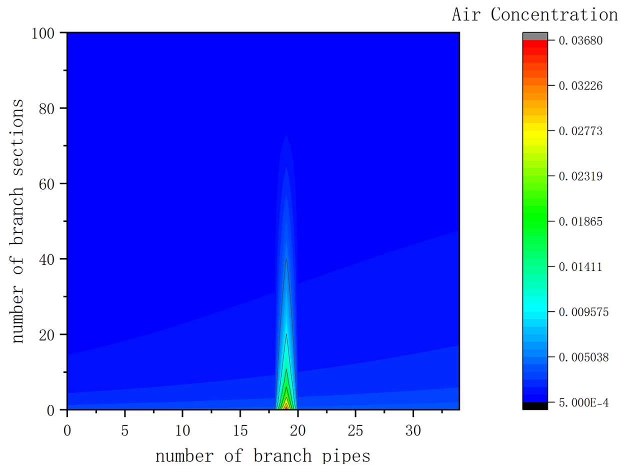

Figure 16: Air concentration distribution of the condensing tube bundle.

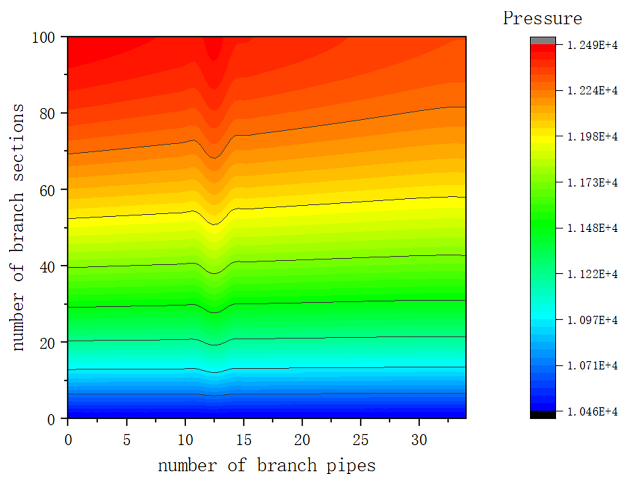

Figure 17: Pressure distribution of the condensing tube bundle.

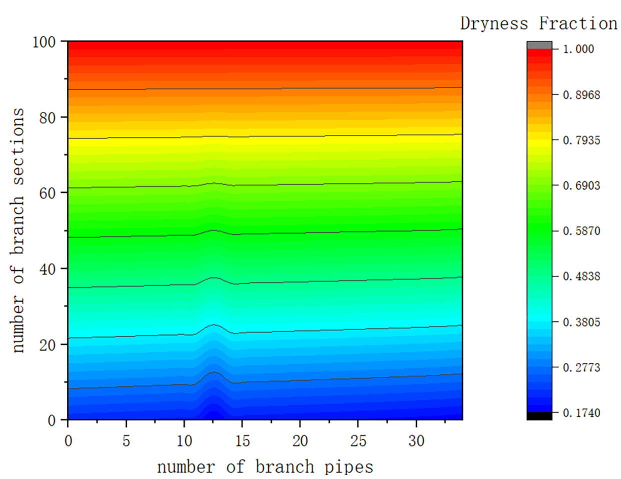

Figure 18: Dryness fraction distribution of the condensing tube bundle.

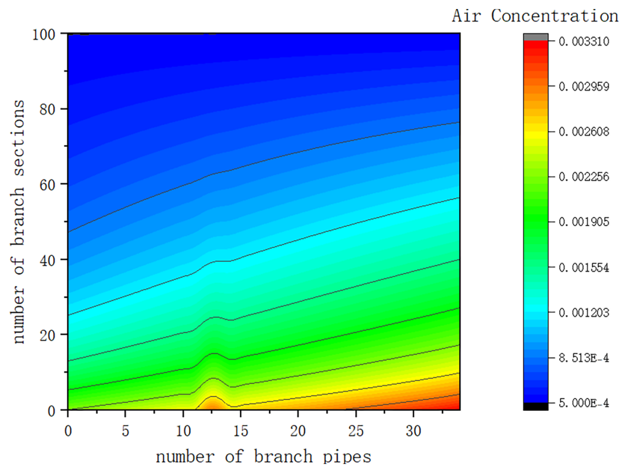

Figure 19: Air concentration distribution of the condensing tube bundle.

Compared to Fig. 6, a distinct difference in the pressure variation trend can be observed within the failed tube bundle region. This deviation is primarily attributed to the deterioration of heat transfer, which reduces condensation efficiency and consequently slows the rate of pressure drop. As a result, at the same axial position, the pressure in the failed bundle region becomes noticeably higher than in the adjacent normal tube bundles. This elevated pressure further leads to a decrease in the amount of steam flowing into the failed bundle.

Locally, the inlet pressure of the failed tube bundle region is higher than that of the adjacent normal regions. This pressure difference leads to a decrease in the steam flow into the failed bundle. Although heat transfer deteriorates and condensation efficiency is reduced within this failed region, the amount of steam requiring condensation is simultaneously lower. Consequently, the outlet dryness fraction in this region remains at a relatively low level.

Globally, the highest condensation degree within the entire tube bundle system corresponds to an outlet dryness fraction of 0.174, which is higher than the value of 0.138 under normal conditions. This is because the excess steam from the failed bundle is diverted to other normal bundles. Under otherwise identical conditions, this redistribution results in a reduced condensation degree and a slight increase in the outlet dryness fraction.

The conclusion derived from Fig. 8 indicates that a region with a higher degree of condensation tends to exhibit a higher air content. This is corroborated in Fig. 11, where the air content at the outlet of the failed region manifests a local maximum. Concurrently, the increased steam inflow into the normal tube bundles reduces their condensation efficiency, thereby decreasing the air-to-total gas ratio. Consequently, as reflected in the data, the maximum air content observed is 0.331%, which is lower than the value of 0.379% under normal operating conditions.

The air mass fraction change is calculated relative to a fixed inlet concentration of 0.05%. The "+0.265%" baseline value means the concentration rises to 0.315% under normal operation. After failure, it rises to 0.294%. The dryness fraction change is calculated based on a fixed inlet dryness fraction of 1. The reference value "−0.840" indicates that the dryness fraction drops to 0.16 under normal operation. After the failure, the dryness fraction drops to 0.175.

According to the data in the Table 1, the failure of a tube bundle creates a localized blockage effect, raising local and inlet pressures. The primary negative effect is a significant increase in system pressure drop

(~15.6%), which directly impacts pumping power requirements. While the redistribution of steam flow leads to a minor beneficial effect on air mass fraction, the overall thermal performance is degraded, as evidenced by the reduced total condensation (higher outlet dryness fraction). The data quantifies the trade-off: the system maintains operation but at a lower efficiency and with a higher energy penalty for fluid circulation.

Table 1: Parameter changes before and after heat exchange failure (taking the 13th condenser tube bundle under the condition of a steam flow rate of 18 t/h and an exhaust air velocity of 10 m/s as an example).

Key Indicator	Pre-Failure Baseline	Post-Failure Simulated Value	Quantitative Change
Condenser Inlet Pressure (Pa)	12,314.1	12,459.3	+145.2
Pressure Drop (Pa)	1848.5	2137.8	+289.3
Air Concentration Change	+0.265%	+0.244%	−0.021%
Dryness Fraction Change	−0.840	−0.825	+0.015

The results suggest that local operating failures not only reduce heat transfer efficiency but also alter the flow distribution characteristics within the ACC system. The increased pressure drop may further hinder steam flow into the affected tube bundles, potentially amplifying performance degradation over a wider area.

The above results demonstrate that the proposed model can capture the coupled effects of heat transfer deterioration, non-condensable gas accumulation, and pressure drop variation under both normal and abnormal operating conditions. The model provides valuable insights into the thermal–hydraulic behavior of ACC systems under local failure scenarios.

From an engineering perspective, the model can be used to identify high-risk tube bundles, diagnose local operating faults, and support the optimization of fan operation strategies and air extraction schemes. Therefore, the proposed modeling framework has practical significance for improving the operational reliability and efficiency of air-cooled condenser systems in large-scale thermal power plants.

4 Conclusions

In this study, a one-dimensional physical model was established for the air-cooled condenser (ACC) system of a 100 MW unit. An iterative numerical method based on the first law of thermodynamics was employed to model and predict the internal condensation heat transfer process. The core of this study lies in making two key corrections to the heat transfer coefficient and analyzing the thermohydraulic characteristics of the system under normal and fault conditions. The main conclusions of this work can be summarized as follows:

(1) An improved condensation heat transfer model was proposed. Most previous models assumed that the air mass fraction remained constant and did not consider the influence of the change in air mass fraction during the condensation process on the model. The author first corrected the widely used Shah horizontal tube condensation correlation by introducing the air mass fraction and Jakob number to quantify the inhibitory effect of non-condensable gases on heat transfer. Secondly, to evaluate the influence of the pipe installation angle, a tilt coefficient (I) was introduced. This coefficient integrates the Eötvös number, Lockhart-Martinelli parameters, and the modified Froude number to correct the heat transfer coefficient in inclined tubes. Additionally, a function for predicting heat loss failure was added, which was not present in the previous model.

(2) The established model can accurately reflect the changes in various parameters under different steam flow rates. As the steam flow rate increases, the degree of steam condensation in the condenser tubes

decreases, the pressure at the tube outlet increases, and the air mass fraction in each part of the tube decreases.

(3) The established model can effectively simulate the system's performance under normal and local fault conditions. Under normal conditions, the model prediction shows that the steam dryness decreases smoothly along the flow direction and the pressure distribution is relatively uniform. When simulating local faults (such as a decrease in the outlet speed of the fan above a specific tube), the model successfully captures phenomena such as deterioration of heat transfer in the fault area, accumulation of non-condensable gases (air), significant increase in pressure drop (for example, the pressure drop increases by approximately 15.6% in the simulation case), and redistribution of steam flow, demonstrating the model's ability to describe the coupling effect between heat transfer, air accumulation, and pressure drop changes.

Acknowledgement: Not applicable.

Funding Statement: The authors received no specific funding for this study.

Author Contributions: Conceptualization, Jiaxi Shen; methodology, Jiaxi Shen; software, Jiaxi Shen and Zhiyun Wang; formal analysis, Jiaxi Shen and Zhiyun Wang; investigation, Jiaxi Shen and Zhiyun Wang; resources, Jiaxi Shen; data curation, Jiaxi Shen; writing—original draft preparation, Jiaxi Shen; writing—review and editing, Jiaxi Shen and Zhiyun Wang; visualization, Jiaxi Shen; supervision, Jiaxi Shen and Zhiyun Wang; project administration, Jiaxi Shen. All authors reviewed and approved the final version of the manuscript.

Availability of Data and Materials: The data that support the findings of this study are available from the corresponding author, Zhiyun Wang, upon reasonable request.

Ethics Approval: Not applicable.

Conflicts of Interest: The authors declare no conflicts of interest.

References

1. Bhagat RD, Deshmukh SJ. Numerical analysis of passive two phase fluid flow in a closed loop pulsating heat pipe. Front Heat Mass Transf. 2021;16(1):1–16. doi:10.5098/hmt.16.23.
2. Yu B, Luo Y, Guo L, Huang L. Flow boiling heat transfer and pressure gradient of R410A in micro-channel flat tubes at 25°C and 30°C. Front Heat Mass Transf. 2025;23(2):553–75. doi:10.32604/fhmt.2025.062851.
3. Yan M, Lu C, Shi P, Zhang M, Zhang J, Wang L. Optimizing two-phase flow heat transfer: DCS hybrid modeling and automation in coal-fired power plant boilers. Front Heat Mass Transf. 2024;22(2):615–31. doi:10.32604/fhmt.2024.048333.
4. Minko KB, Artemov VI, Klement'ev AA. Simulation of condensation of stagnant or moving saturated vapor on a horizontal tube using the volume-of-fluid (VOF) method. Therm Eng. 2023;70(3):175–93. doi:10.1134/S0040601523030059.
5. Duan Z, Tian Y, Wang S, Long L, Deng J. Research on fluid flow and heat transfer characteristics in a three-dimensional condenser. Ann Nucl Energy. 2025;211:110967. doi:10.1016/j.anucene.2024.110967.
6. Minko KB, Yankov GG, Artemov VI, Ptakhin AV. Simulation of halon condensation processes in vertical pipes by the VOF method. Therm Eng. 2023;70(7):534–49. doi:10.1134/S0040601523070042.
7. Mirzabeygi P, Zhang C. Turbulence modeling for the two-phase flow and heat transfer in condensers. Int J Heat Mass Transf. 2015;89:229–41. doi:10.1016/j.ijheatmasstransfer.2015.05.044.
8. Mirzabeygi P, Zhang C. Three-dimensional numerical model for the two-phase flow and heat transfer in condensers. Int J Heat Mass Transf. 2015;81:618–37. doi:10.1016/j.ijheatmasstransfer.2014.10.015.

9. Minko KB, Yankov GG, Artemov VI, Milman OO. A mathematical model of forced convection condensation of steam on smooth horizontal tubes and tube bundles in the presence of noncondensables. Int J Heat Mass Transf. 2019;140:41–50. doi:10.1016/j.ijheatmasstransfer.2019.05.099.
10. Nada SA, Hussein HMS. General semi-empirical correlation for condensation of vapor on tubes at different orientations. Int J Therm Sci. 2016;100:391–400. doi:10.1016/j.ijthermalsci.2015.10.023.
11. Shah MM. New correlation for heat transfer during subcooled boiling in plain channels and annuli. Int J Therm Sci. 2017;112:358–70. doi:10.1016/j.ijthermalsci.2016.10.016.
12. Yang P, Cao X, Liu J, Zhou S. Experimental study of steam condensation heat transfer in an inclined tube at low mass fluxes. Int J Heat Mass Transf. 2024;224:125257. doi:10.1016/j.ijheatmasstransfer.2024.125257.
13. Mohseni SG, Akhavan-Behabadi MA. Visual study of flow patterns during condensation inside a microfin tube with different tube inclinations. Int Commun Heat Mass Transf. 2011;38(8):1156–61. doi:10.1016/j.icheatmasstransfer.2011.04.032.
14. Lee YW, Ho JY, Leong KC, Wong TN. A theoretical study of condensation heat transfer in tubes with novel cross-sections. Therm Sci Eng Prog. 2022;28:101075. doi:10.1016/j.tsep.2021.101075.
15. Yang JG, Ju XL, Ye S. An empirical correlation for steam condensing and flowing downward in a 50 mm diameter inclined tube. Adv Mater Res. 2013;732:67–73. doi:10.4028/www.scientific.net/amr.732-733.67.
16. Lips S, Meyer JP. Stratified flow model for convective condensation in an inclined tube. Int J Heat Fluid Flow. 2012;36:83–91. doi:10.1016/j.ijheatfluidflow.2012.03.005.
17. Minko KB, Yankov GG, Artemov VI. Numerical simulation of the formation process of zones with increased air content in tube bundles during condensation of steam containing small concentrations of air. Therm Eng. 2022;69(4):252–8. doi:10.1134/s0040601522040048.
18. Yang LJ, Chen L, Du XZ, Yang YP. Effects of ambient winds on the thermo-flow performances of indirect dry cooling system in a power plant. Int J Therm Sci. 2013;64:178–87. doi:10.1016/j.ijthermalsci.2012.08.010.
19. Anwar Z, Palm B, Khodabandeh R. Flow boiling heat transfer, pressure drop and dryout characteristics of R1234yf: experimental results and predictions. Exp Therm Fluid Sci. 2015;66:137–49. doi:10.1016/j.expthermflusci.2015.03.021.
20. Jatau T, Bello-Ochende T. Numerical investigation and entropy generation for flow boiling evaporation in U-bend tube heat exchanger with elliptical and circular cross-sections. Therm Sci Eng Prog. 2022;35:101480. doi:10.1016/j.tsep.2022.101480.
21. Chang W, Li W, Ma J, Luo K, Li C. Enhanced flow boiling in microchannels integrated with hierarchical structures of micro-pinfin fences and nanowires. Langmuir. 2021;37(30):8989–96. doi:10.1021/acs.langmuir.1c00891.
22. Aroonrat K, Wongwises S. Experimental investigation of condensation heat transfer and pressure drop of R-134a flowing inside dimpled tubes with different dimpled depths. Int J Heat Mass Transf. 2019;128:783–93. doi:10.1016/j.ijheatmasstransfer.2018.09.039.
23. Kang P, Heo J, Yun R. Condensation heat transfer characteristics of CO_2 in a horizontal smooth tube. Int J Refrig. 2013;36(3):1090–7. doi:10.1016/j.ijrefrig.2012.10.005.